Journal of Materials Chemistry C

Accepted Manuscript

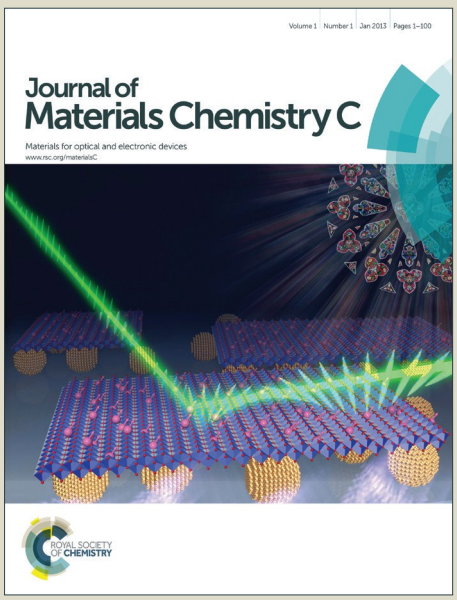

ROYAL SOCIETY OF CHEMISTRY

www.rsc.org/materialsC

A highly efficient, orange light-emitting $(K_{0.5}Na_{0.5})NbO_3:Sm^{3+}/Zr^{4+}$ lead-free piezoelectric material with superior water resistance behavior

Qiwei Zhang[1], Ke Chen[2], Leilei Wang[1], Haiqin Sun [1*], Xusheng Wang[3], Xihong Hao[1]

[1] School of Materials and Metallurgy, Inner Mongolia University of Science and Technology, 7# Arerding Street, Kun District, Baotou 014010, China

[2] Key Laboratory for Special Functional Materials of Ministry of Education, Henan University, Kaifeng 475004, China

[3] Functional Materials Research Laboratory, School of Materials Science and Engineering Tongji University, 4800 Caoyang Road, Shanghai 201804, China

Abstract

Multifunctional luminescent materials based on rare earth doped ferro-/piezoelectrics have attracted much attention due to their potential applications in novel multifunctional devices. Currently, it remains a challenge to fabricate these materials with high photoluminescence quantum yields, comparable to values obtained for traditional phosphors. Herein, we reported a highly efficient, orange light-emitting material with a superior water resistance behavior based on a $(K_{0.5}Na_{0.5})NbO_3$ (KNN) matrix co-doped with Sm^{3+} and Zr^{4+}. The phase structure, composition, photoluminescence property, thermal quenching and water resistance behavior of the samples were systematically studied. A significantly enhanced orange light-emission at 597 nm originating

[1*] Corresponding author: Tel.: +86 472 6896872; Fax: +86 472 5951571

E-mail: a8082sz@imust.edu.cn (H. Sun). 2 author contributed equally to this work.

from the $^4G_{5/2}\rightarrow{}^6H_{7/2}$ transition of Sm^{3+} was observed by the introduction of Zr^{4+} ions, which can be well explained by the exchange charge model of crystal field. Particularly we achieve a photoluminescence quantum yield as high as 53% and superior water resistance property almost maintaining the same PL intensity as before immersion after 80 h water immersion time for the composition of $(K_{0.5}Na_{0.5})_{0.99}Sm_{0.01}Nb_{0.09}Zr_{0.01}O_3$ under 407 nm n-UV light excitation. The QY value can be comparable to some commercial phosphors, such as $Y_2O_2S/Y_2O_3:Eu^{3+}$. These findings show great potential of the Sm^{3+}/Zr^{4+} co-doped KNN material for a future application in white LEDs and novel multifunctional devices.

Keywords**:** Luminescent materials; Ferro-/piezoelectrics; Quantum yields; Water resistance

1. Introduction

Among all lead-free piezoelectric materials, such as $BaTiO_3$ (BT), $(Bi_{0.5}Na_{0.5})TiO_3$) (BNT) and their derivatives, $(K_{0.5}Na_{0.5})NbO_3$ (KNN) is currently one of the most widely exploited materials since a significant breakthrough made by Saito et al. in 2004, which exhibits an excellent piezoelectric coefficient (d_{33}) comparable to values obtained for $Pb(Zr,Ti)O_3$.[1] Sodium potassium niobate (KNN) is a solid solution of ferroelectric $KNbO_3$ and anti-ferroelectric $NaNbO_3$ in the ratio of 1:1 with an $A^{1+}B^{5+}O_3^{2+}$ perovskite structure. At room temperature, it has a coexisted crystal structure with both tetragonal and orthorhombic ferroelectric phases. With increasing temperatures, it exhibits several phase transitions similar to end member of the solid solution ($KNbO_3$).[2-5] And, these phase transition temperatures can be easily shifted by varying K/Na mole ratio or chemical doping (A-site and/or B-site substitution), then leading to the movement of the orthorhombic and tetragonal phase transition temperature toward room temperature ($T_{O\text{-}T}$), known as polymorphic phase transition (PPT). The presence of PPT favors the enhancement of piezoelectric properties, for example, Li, Ag, RE(rare-earth elements), and Ba dopants at A-site, Ta, Sb, Zr, etc. dopants at B-site.[6-11] Therefore, the majority of studies on KNN-based ceramics focus on an enhancement of the piezoelectric property and a practical application in micro-electronic devices, such as smart sensors, actuators, and piezoelectric transducers etc..[12]

Along with the intensive development of microelectronic devices toward miniaturization, light weight, and integration, researchers would like to discover some materials or devices, which can realize multiple functions. For example, the coexistence of ferromagnetism, ferroelectricity, and magnetoelectric coupling is observed in magnetoelectric and multiferroic materials.[13,14] It is known that rare earth elements (Lanthanide) are commonly used to fabricate high efficient

luminescent materials as activator ions, or improve mechanical and electrical properties as structural modifiers.[15,16] In 1997, Diallo et al. reported a strong single red emission (613 nm) at room temperature in Pr^{3+}-doped $CaTiO_3$ ferroelectric material. Subsequently, the filled ferroelectric materials with RE ions attracted considerable attention owing to the particular luminescence, dielectric and ferroelectric properties.[17] In 2005, Wang et al. fabricated high electrostrictive strain, strong mechanoluminescence and electroluminescence material in Pr^{3+}-doped $(1-x)BaTiO_3$-$xCaTiO_3$ ceramics, which paves the way for developing new multifunctional materials and high-performance single functional materials.[18] Since then, multifunctional luminescent materials have stimulated an increasing practical interest, considerable efforts have been made to search for the potentials of rare-earth doped functional hosts (ferroelectric or piezoelectrics), combining light emission with their intrinsic ferroelectricity, piezoelectricity, or electro-optic properties, as shown in Fig. 1.[19,20]

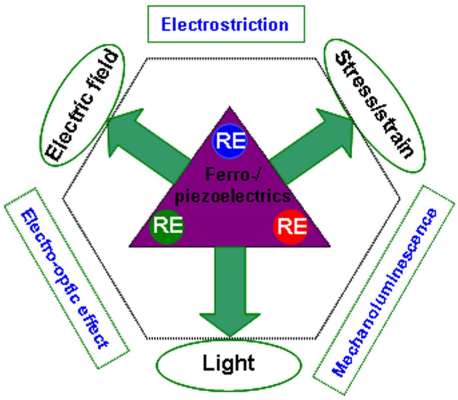

Fig. 1. Schematic illustation of multiple functions of RE-doped ferro-/piezoelectrics.

Nowdays, several studies on RE-doped ferroelectric oxides have been reported, these experiments show that the simultaneous existence of luminescence and ferro-/piezoelectric properties may be realized by controlling the host and rare earth-ion dopants.[21,22] For example, in Pr^{3+}-doped KNN host, a dual-enhancement of both the ferro-/piezoelectric and the

photoluminescence performance can be realized.[23] Unfortunately, low luminescence efficiency in RE-doped ferro-/piezoelectric oxides is up to now still a difficult problem that some researchers face due to their larger phonon energies. In contrast, traditional phosphors, such as alkaline earth sulfide/oxysulfide phosphors and nitrides/oxynitrides with low phonon energies are beneficial to decrease non-radiative relaxation losses and increase the overall metastable energy lifetime, resulting in high luminescence efficiency (quantum yield > 90%).[24-26] To further improve the luminescence efficiency of RE-doped ferro-/piezoelectric oxides, two important strategies have been widely adopted: (i) applying electric field, strain, polarization or photons in ferro-/piezoelectric oxides and (ii) substitution of ions at A site or B site.[27-29] So far, achieving high-efficient RE-doped ferro-/piezoelectric materials to values comparable to traditional phosphors still remains a big challenge, only a few studies have been reported on this aspect. In addition, an understanding of luminescence mechanism for high-efficient RE-doped ferro-/piezoelectric materials would be highly beneficial to materials design and fabrication for future integrated optoelectronic devices.

Our previous results have shown that KNN is a promising host matrix for luminescent materials achieved through the introduction of rare earth (RE) ions, due to their superior chemical stability, successive structural phase transitions, wide band gap and non-linear optical behavior.[30,31] Generally, luminescence coming from 4f-4f transitions of RE ions are both parity forbidden, whereas the parity selection rules will be broken as RE ions are embedded in low symmetry hosts, leading to the increase of transition probabilities of energy levels of RE ions.[32] Therefore, combining some features of KNN materials mentioned above, it is possible to design and fabricate highly efficient luminescent ferro-/piezoelectric materials by the introduction of RE

ions into KNN host. In the present study, we report a highly efficient, orange light-emitting material based on a $(K_{0.5}Na_{0.5})NbO_3$ (KNN) matrix co-doped with Sm^{3+} and Zr^{4+} ions, and investigate the more detailed crystal structure, photoluminescence properties, thermal stability, and its water resistance behavior. The characteristics suggest that the Sm^{3+}/Zr^{4+} co-doped KNN material is a promising orange phosphor with superior water resistance behavior for application in W-LEDs with near-UV-LED chips (380-420 nm), and may have great potential in novel multifunctional devices.

2. Material and methods

2.1. Sample preparation

$(K_{0.5}Na_{0.5})_{0.99}Sm_{0.01}Nb_{1-x}Zr_xO_3$ (abbreviated as $KNSNZ_x$, x=0, 0.002, 0.005, 0.008, 0.010, 0.015) samples were prepared by conventional solid-state reaction techniques. Highly purified metal oxides or carbonates are used as raw materials: K_2CO_3 (99%, Alfa Aesar), Na_2CO_3 (99.5%, Alfa Aesar), Nb_2O_5 (99.5%, Alfa Aesar), Sm_2O_3 (99.99%, Alfa Aesar) and ZrO_2 (99.975%, Alfa Aesar). The weighted powders according to stoichiometric ratio were mixed with ethanol, dried, calcined at 880 °C for 6 h in air. After the calcination, $KNSNZ_x$ powders were remixed and then dried. Subsequently, the dried powders were granulated with 8 wt% polyvinyl alcohol (PVA) binder, and pressed into disk-shaped pellets with diameter of 10 mm at 100 MPa. The green pellets of $KNSNZ_x$ were heated at 550 °C to burn off the PVA. It is known that KNN-based materials are difficult to density by normal sintering methods due to alkaline volatilization during sintering. So, in this paper, the green pellets with different compositions were sintered at various temperatures from 900 to 1200 °C and different holding times from 1h to 10 h to obtain the optimized processing. The samples were sintered at 1160 °C (x=0), 1170 °C (x=0.002), 1150 °C (x=0.005,

0.008, 0.010), and 1140 ºC (x=0.015), respectively, and held time for 4h.

The sintered pellets were polished to a thickness of 0.5 mm for the measurements of the photoluminescence (PL) and photoluminescence excitation (PLE) spectra. The quantum yield and decay samples were prepared using the sintered ceramic powders. The water resistance samples were fabricated by the following procedure:. The ceramic powder (0.4 g) was dispersed in distilled water (20 ml) by sonication and magnetic stirring for 20 min, the dispersed powder was placed in distilled water for 0, 10 h, 20 h, 40 h, 60 h and 80 h, respectively. Afterwards, the mixed powders were dried at 100 °C.

2.2. Characterization

The sample crystal structure was investigated by powder X-ray diffraction (XRD) analysis (D8 Advanced, Bruker, Germany) with Cu Kα radiation (λ=1.5418 Å). The inductively coupled plasma atomic emission spectroscopy (ICP-AES) (PROFILE SPEC, Leeman, AMERICA) was adopted to quantitatively investigate the composition deviation behavior of K and Na in KNN host, 50 mg samples quantitatively dissolved in 50ml flask (3%HNO_3) were used to test the composition content of samples. The photoluminescence (PL) and photoluminescence excitation (PLE) spectra of ceramic or powder samples at room temperature were tested by a spectrofluorometer (F-4600, HITACHI, Japan) with a xenon lamp. The temperature-dependence properties of photoluminescence samples were measured using a Hitachi F-4600 equipped with a temperature-controlled chamber (Linkam, THMS600, United Kingdom). The diffuse reflectance spectra were taken on a UV/Vis spectrophotometer (U-3900, HITACHI, Japan). The quantum yield and decay curves of the samples were obtained by a combined steady state & time resolved fluorescence spectrometer (FLS920, Edinburgh Instruments, United Kingdom).

3. Results and discussion

3.1. Phase structure and composition

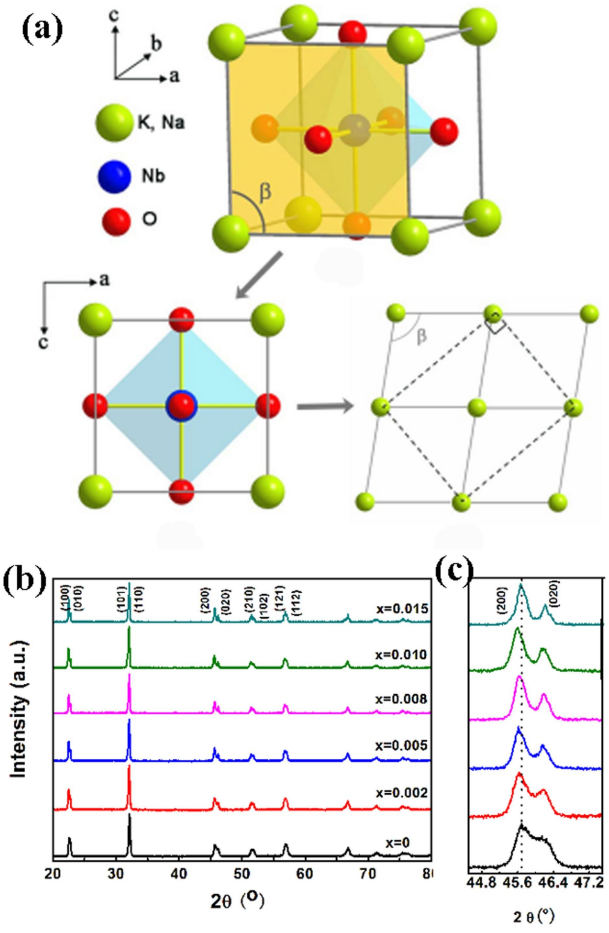

Fig. 2 (a) The illustation of KNN with orthorhombic structure at room temperature [Ref. 3], (b) XRD patterns of $KNSNZ_x$ ceramics and (c) XRD patterns for the (200) and (020) peaks from 44° to 47.5°.

The crystal structure of pure KNN at room temperature is an orthorhombic structure with the space group *Amm*2, while the perovskite-type ABO_3 primary subcell has monoclinic symmetry, where lattice parameters are $a_m=c_m>b_m$, as illustrated in Fig. 2(a). It is known that the a_m and c_m axes equal to each other ($a_m=c_m$), and b_m axis is perpendicular to $a_m=c_m$ plane, its interaxial angle β is almost close to 90°.[3] The x-ray diffraction patterns of $(K_{0.5}Na_{0.5})_{0.99}Sm_{0.01}Nb_{1-x}Zr_xO_3$ ceramics

are presented in Fig. 2(b). It can be seen from the Fig 2(b), only a single phase perovskite structure with orthorhombic symmetry is observed in all $KNSNZ_x$ samples, which can be indexed by standard PDF card of $KNbO_3$ (PDF#32-0822), there are no significant differences between diffraction patterns, similar to some results reported by Lin et al..[33] The diffraction peaks of ceramic samples are slightly shifted to the lower angle side with increasing Zr^{4+}-doped content up to x=0.01 due to the relatively larger ionic radius of Zr^{4+} [0.72 Å, CN=6] compared to Nb^{5+} [0.64 Å, CN=6], resulting in an expansion of KNN cell volumes.[34] While, the sample with high Zr levels show a shift to higher angle due to the occurrence of vacancies, the detailed origin was given in the following section. This shifting effect can be seen more clearly in the XRD patterns for the (200/020) characteristic peaks at a 2θ of $\sim 45.5^{o}$, and the distance of the location of (200) and (020) is enlarged with the Zr content, indicating that the phase structure transitions occur from orthorhombic structure to tetragonal structure, as shown in Fig. 2(c). These results also implies that the Sm^{3+} and Zr^{4+} ions have entered into the unit cell of KNN host maintaining the perovskite-type ABO_3 structure. Based on the ionic radius and the ions' charges, we believe that Zr^{4+} ions tend to occupy the B sites in ABO_3 structure. And, all samples were well sintered at different sintered temperatures and exhibited dense microstructure with relatively high densities (>94%) and well-grown grains with any apparent second phase (see Fig.1S).

The measured infrared (IR) reflectivity spectra of several representative samples of $KNSNZ_x$ (x=0, 0.002, 0.008, 0.015) at room temperature are shown in Fig. 3. For all composition samples, the IR spectra show a broad strong band centered at about 659 cm^{-1} and a weak band centered at about 3416 cm^{-1}. The presence of these two bands indicates the formation of the perovskite phase, which is in good agreement with the XRD results in Fig. (2). It is interesting to note that there is

an additional band to appear near 1642 cm^{-1} when Zr^{4+} ions are doped to B sites of KNN host. The additional band at～1642 cm^{-1} is probably related to the vibration of the Zr-O bond due to the Zr^{4+} substitution to Nb^{5+} in the ABO_3 structure.[35]

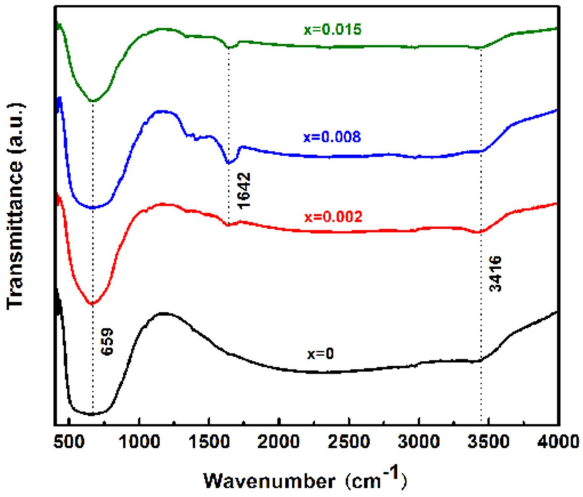

Fig. 3. IR spectra of the $KNSNZ_x$ (x=0, 0.002, 0.008, 0.015) at room temperature

In general, the volatilization of alkali elements in KNN-based ceramics is generally unavoidable during sintering, because of their relatively high sintering temperature (over 1000 ºC) close to its melting point at 1200 ºC. The volatilization behaviors certainly generate compositional fluctuation, namely K/Na mole ratio, and could influence the piezoelectric and luminescent performances.[2,36] So, it is necessary to quantitatively determine the volatilization degree and mole ratio of K/Na. For this purpose, the inductively coupled plasma atomic emission spectroscopy (ICP-AES) is used to investigate the loss degree and stoichiometric deviation behaviors. Fig. 4 gives the weight percentage and K/Na mole ratio of alkali elements (K, Na) as a function of Zr^{4+} concentrations in $KNSNZ_x$ (x=0.002, 0.010, 0.015) ceramic samples. The chemical composition data of K and Na are listed in Table 1. According to the atomic weight of K and Na, the K/Na mole ratio can be accurately calculated. From the Table 1 and Fig. 4, the K/Na mole ratio shows

an apparent deviation from 1, and the values of K/Na mole ratio gradually increase with the increase of Zr concentrations up to x=0.01. The apparent deviation from stoichiometry ratio indicates clearly that Na elements volatilize more seriously than K elements. Further increasing Zr contents lead to the decrease of K/Na mole ratio close to 1. The abnormal results compared to low Zr doped levels means that the Zr dopants could inhibit the volatilization degree of Na elements to some extent, the exact origins still need further studies in the future.

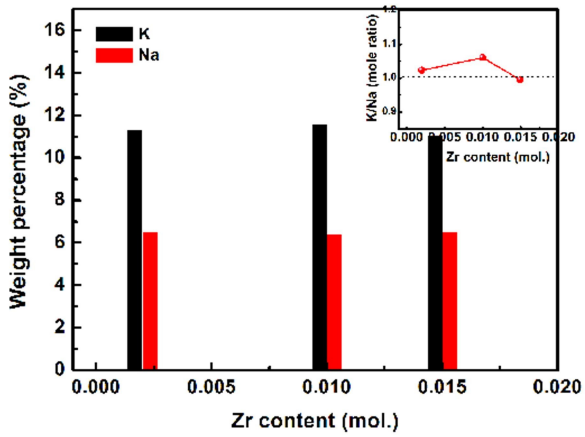

Fig. 4. Weight percentage and K/Na mole ratio as a function of Zr^{4+} concentrations in $KNSNZ_x$ (x=0.002, 0.010, 0.015) ceramic samples.

3.2. Photoluminescence property

Sm^{3+} ions are currently used in most commercial phosphors as activators, showing orange-red light-emission at about 610 nm.[37,38] The light-emission intensity can be remarkably enhanced by introducing compensator or sensitizer ions (lanthanide or mental ions), which can effectively compensate for the low luminescence efficiency of RE ions resulting from the small absorption cross section of the parity-forbidden intra-4f transition.[39,40] As we are expected, chemically stable Zr^{4+} ions more favor transition probabilities of energy levels of Sm^{3+} ions in the present study. Fig. 5 shows the PL excitation and emission spectra of the $KNSNZ_x$ (x=0, 0.01) ceramic samples at

room temperature together with the reflection spectra of $KNSNZ_x$ (x=0.01) sample. From the shape and position of the excitation and emission peaks, the introduction of Zr^{4+} ions have no influence on the PL and PLE patterns, except for significantly enhancing the relative intensity. In Fig. 5, the PLE spectra monitored at 597 nm show five sharp absorption bands range from 380 to 500 nm, which are located at 407 nm, 419 nm, 439 nm, 463nm, and 479 nm, respectively. The strongest absorption appears in the near UV region of 407 nm, whose band covers the emission wavelength of the commercial n-UV LED chips (360-410 nm). According to the energy level scheme of Sm^{3+}, these sharp excitation peaks is mainly caused by the typical f-f transition from the $^6H_{5/2}$ absorption to the $^4F_{7/2}$, $^4P_{5/2}$, $^4G_{9/2}$, $^4I_{13/2}$ and $^4I_{11/2}$ excited states of Sm^{3+} ions, corresponding to $^6H_{5/2}\rightarrow{}^4F_{7/2}$ (407 nm), $^6H_{5/2}\rightarrow{}^4P_{5/2}$ (419 nm), $^6H_{5/2}\rightarrow{}^4G_{9/2}$ (439 nm), $^6H_{5/2}\rightarrow{}^4I_{13/2}$ (463 nm), and $^6H_{5/2}\rightarrow{}^4I_{11/2}$ (479 nm) transitions, respectively. The locations of the PLE peaks are almost coinciding with the diffuse reflection spectrum of $KNSNZ_x$ (x=0.01) sample, similar behavior can be also observed in other Zr^{4+}-doped samples (not shown here). When the samples are excited by 407 nm, the obtained PL spectra consist of three bands: a green emission at 546～580 nm, a red emission at 580～679 nm, a much weaker infrared band emission at 690～740 nm. These emission peaks are mainly originating from the transitions of the excited state $^4G_{5/2}$ levels to the ground state $^6H_{5/2}$, $^6H_{7/2}$, $^6H_{9/2}$, and $^6H_{11/2}$ levels through the nonradiative relaxation of the excited state $^4G_{7/2}$ to the $^4G_{5/2}$ state, attributed to the characteristic f-f transition of Sm^{3+} from the $^4G_{5/2}\rightarrow{}^6H_{5/2}$ transition at 564 nm, $^4G_{5/2}\rightarrow{}^6H_{7/2}$ transition at 597 nm, $^4G_{5/2}\rightarrow{}^6H_{9/2}$ transition at 647, and $^4G_{5/2}\rightarrow{}^6H_{11/2}$ transition at 710 nm, respectively. In addition, the emission spectra excited by different wavelength (407 nm, 419 nm, 439 nm, 463 nm, and 479 nm) are shown in the inset of Fig. 5. The emission peak positions and patterns have no changes except for their relative

intensities, indicating an effective energy transfer from the absorptions at the excited bands to the $^4G_{5/2}\rightarrow{}^6H_{7/2}$ emission.

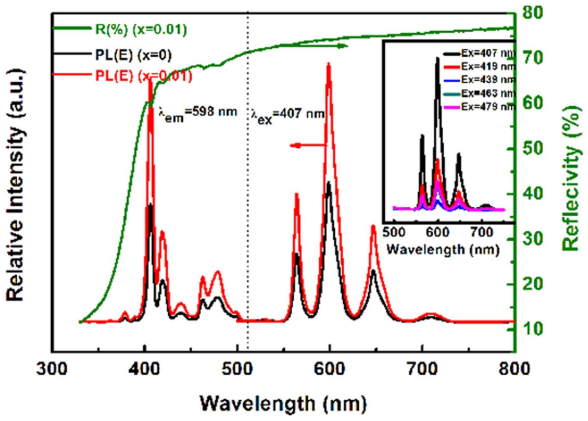

Fig. 5. Room temperature PLE, PL and diffuse reflectance spectra of the $KNSNZ_x$ (x=0, 0.010) ceramics. The inset is the PL spectra of sample (x=0.10) excited by different wavelength.

In order to investigate the effect of Zr^{4+} doping concentrations on the emission intensity, we have prepared a series of Zr^{4+} doped samples ($KNSNZ_x$, x=0, 0.002, 0.005, 0.008, 0.010, 0.015), and obtained the emission spectra of samples excited at 407 nm, as shown in Fig. 6. As can been seen from Fig. 6, the PL intensity increases gradually with the increase of Zr^{4+} concentrations, and reaches a maximum when the doped content x is up to 0.01 mol. In the inset of Fig. 6, the dependence of the $^4G_{5/2}\rightarrow{}^6H_{7/2}$ emission intensity on Zr^{4+} concentrations clearly shows the strongest orange emission with 0.01 mol Zr^{4+} addition, with an increase of almost 202% compared to the samples without Zr^{4+} doping. However, the emission intensity greatly decreases with further increasing Zr^{4+} content due to concentration quenching. These results mean that there exists a nonradiative energy transfer between Sm^{3+} and Zr^{4+} ions by exchange interaction, radiation reabsorption or multipole-multipole interaction owing to the variations of local crystal field symmetry. Similar results were reported by Ramasamy et al. in Fe^{3+} doped β-$NaGdF_4$:Er-Yb

materials.[41] For the present samples, Zr^{4+} ionic doped KNSN at B sites induces the local lattice distortion, then reduces the local crystal field symmetry too. So, the breaking of local crystal field symmetry plays a dominating role in an enhancement of the emission intensity, although there is no sufficient evidence to support it. Nevertheless, the experimental data (the enhanced PL and no shift of emission peaks) show that Zr^{4+} substitution does give rise to distinct influence to the excitation, emission intensity, and crystal structure.

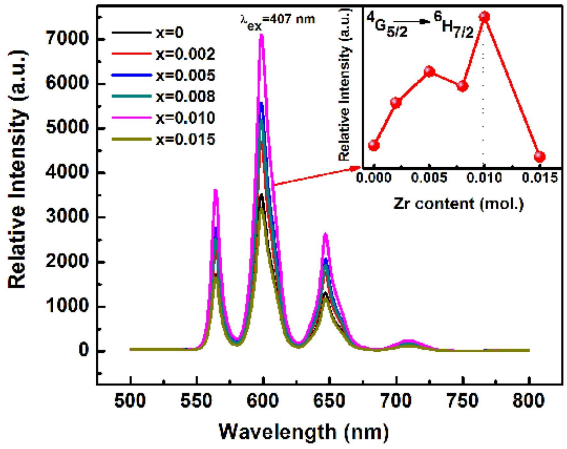

Fig. 6. PL spectra of $KNSNZ_x$ ceramics excited by 407 nm at room temperature, the inset is the dependence of the emission intensity ($^4G_{5/2}\rightarrow{}^6H_{7/2}$) on Zr^{4+} concentrations.

According to the exchange charge model of crystal field proposed by Malkin et al.,[42] the energy level distribution of Sm^{3+} may be described by the eigenvalues of the crystal field Hamiltonian:

$$H = \sum_{p=2,4} \sum_{k=-p}^{p} B_p^k O_p^k \qquad (1)$$

Where B_p^k is a crystal field parameter representing the information of the geometrical structure of an impurity center, for example, the covalent bond and exchange interaction. O_p^k is the linear combinations of irreducible tensor operators acting on angular parts of the Sm^{3+} ion wave

functions. According to the results described in Fig. 2, the Zr^{4+} substitution causes an expansion of the perovskite lattice due to the relatively larger ionic radius of Zr^{4+}, the distances for Sm^{3+}-O^{2-} bond become longer, and the crystal field parameters B_p^k become smaller, then resulting in a significant enhancement of the emission intensity by inhibiting a nonradiative energy transfer from one Sm^{3+} to another through exchange interaction, namely the occurrence of concentration quenching. In contrast, the emission intensity seriously decreases as the Zr^{4+} concentration arrives to be 0.015 mol, originating from the increase of the local crystal field symmetry due to the shrinkage of cell volumes, as observed in Fig. 2. It is found that the (200) diffraction peak of sample with x=0.015 mol shifts to higher angle side, which can be readily attributed to the appearance of the vacancy-related defects. The formation of the vacancy-related defects can be written as follows:

$$5Sm^{3+}(-K_{0.5}Na_{0.5}) \rightarrow 5S\ddot{m}_{(K_{0.5}Na_{0.5})} + 2V_{Nb}''''' \qquad (2)$$

$$2Zr^{4+}(-Nb_2O_5) \rightarrow 2Zr'_{Nb} + 5O^{\times} + \ddot{V}_O \qquad (3)$$

In present study, the positive-charge defects $(Sm_{K0.5Na0.5})^{2+}$ can effectively compensate for the negative-charge defects $(Zr_{Nb})^{-}$ when the Zr^{4+} concentrations are below 0.020 mol. Therefore, it is impossible to form oxygen vacancies according to the Eq. (3). As shown in Fig. 7, the residual positive-charge defects $(Sm_{K0.5Na0.5})^{2+}$ would be neutralized by the formation of Nb vacancies (V_{Nb}). With the increase of Zr^{4+} concentrations, a great deal of Nb vacancies will induce the shrinkage of cell volumes, leading to the shift of (200) diffraction peak to higher angle side. In addition, the charge compensation behavior is known to significantly improve the emission intensity of luminescent materials. However, in Zr^{4+} doped KNSN samples, the emission intensity reaches its maximum at x=0.010 mol, here, the positive-charge defects $(Sm_{K0.5Na0.5})^{2+}$ with 0.01

mol Sm^{3+} are only partially compensated for the negative-charge defects $(Zr_{Nb})^{-}$, suggesting that there is another important mechanism, the breaking of the local crystal field symmetry discussed above, to favor the improvement of emission intensity except for the charge compensation. Therefore, we believe that the significant enhancement of the light-emission with increasing Zr^{4+} concentration can mainly be ascribed to the breaking of local crystal field symmetry.

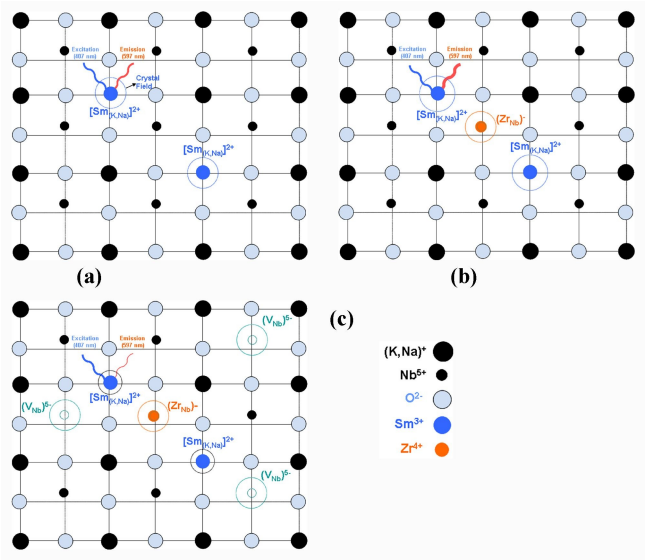

Fig. 7. Variations of local crystal field and vacancy formation in KNN host co-doped with Sm^{3+} and Zr^{4+}, (a) x=0, (b) x≤ 0.01, (c) x>0.01

Several studies have confirmed that KNN-based ceramics are mostly fabricated within a narrow processing window (～10 ºC) in terms of the sintering temperature, and the obtained samples have low density and poor microstructure, which definitely degrades piezoelectric or ferroelectric performance.[43] Similarly, the PL properties of RE-doped luminescent materials are also strongly influenced by these factors, as like the results reported by many researchers.[44,45] Based on the above considerations, it is necessary to study the optimal condition of normal sintering of $KNSNZ_x$ ceramics and influence of sintering condition on PL properties. In order to obtain the optimal processing, we present the effects of the sintering temperature and holding time on PL

performance for the representative $KNSNZ_x$ (x=0.010) composition, as shown in Fig. 8 (a) and (b). The emission spectra excited by 407 nm display similar shape and no shift of peaks to the results observed in Fig. 5. The strongest emission peak still appears at 597 nm ($^4G_{5/2}\rightarrow{}^6H_{7/2}$). The relative intensity dependence of the $^4G_{5/2}\rightarrow{}^6H_{7/2}$ transition on sintering temperature from 900 ^{o}C to 1200 ^{o}C is shown in the inset of Fig. 8 (a). We can clearly observe a significant increase of the emission intensity with increasing sintering temperature up to 1130 ^{o}C, and then decreases once the temperature exceeds 1130 ^{o}C. These results indicates that the nucleation rate and crystallite growth gradually increase during the formation of KNN pervoskite phase when the sintering temperature is lower than 1130 ^{o}C, which is beneficial to improve the emission intensity, while at temperature higher than 1130 ^{o}C, the serious volatilization of K and Na elements and compositional deviation from the intended stoichiometry (K/Na=1), as illustrated in Fig. 4, might destroy the crystal structure of KNN host.[46] Meanwhile, the samples seem to be oversintered and melted, then leading to the decreased emission intensity. Likewise, a proper holding time at a high sintering temperature (1130 ^{o}C) also enhances the emission intensity, as shown in Fig. 8 (b). At that time, the density and crystallite degree will reach their maximum. A longer holding time (higher than 4h) brings about the higher degree of volatilization of K and Na ions, so the emission intensity decreases. As mentioned above, the PL performance of the $KNSNZ_x$ system can be well tailored by modifying the processing condition. The optimized process in this study is obtained for 0.01 mol of Zr^{4+}, a sintering temperature of 1130 °C , and a holding time of 4h.

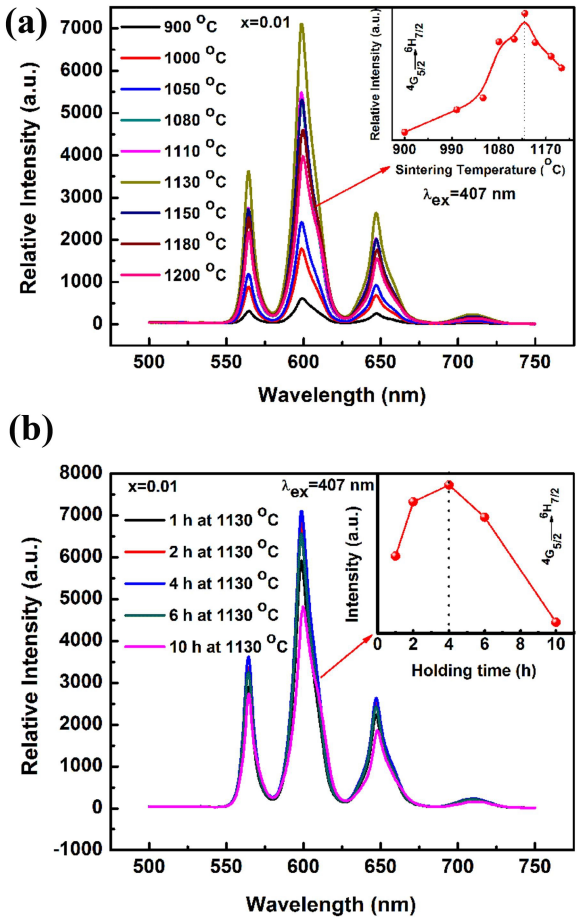

Fig. 8. PL spectra of the KNSNZ$_x$ (x=0.01) ceramics at different sintering temperature (a) and holding time (b) excited by 407 nm at room temperature, the insets show the dependence of emission intensity ($^4G_{5/2}\rightarrow{}^6H_{7/2}$) on sintering temperature and holding time.

The absolute PL quantum yield (QY) is a key parameter to quantitatively evaluate the light-emission intensity, defined as the ratio of emitted photons to absorbed photons. The QYs of the KNSNZ$_x$ samples at room temperature are measured using a combined steady state & time resolved fluorescence spectrometer (FLS920), the obtained results are listed in Table 1. It can be seen that the samples doped with Zr^{4+} ions show high PL QYs ranging from 0.40 to 0.53. Especially, the sample with 0.010 mol Zr^{4+} exhibits the best result, the QY value reaches 0.53, which is superior to the recently reported QY values of RE-doped ferro-/piezoelectric

materials,[17,18,21,23,47] and comparable to some commercial phosphors, such as $Y_2O_2S/Y_2O_3:Eu^{3+}$.[48] Since the QY is closely correlated to the microstructure, processing conditions, the particle/grain size, and crystallinity of materials, the higher QYs can be obtained by further optimization for $KNSNZ_x$ system. Meanwhile, the luminescence decay curves at room temperature are measured for $KNSNZ_x$ samples (x=0, 0.002, 0.005, 0.008, 0.010, 0.015) (excitation at 407 nm, emission at 597 nm) as shown in Fig. 9, the decay profiles can be well fitted by a double exponential fit, and the average decay lifetimes (τ) can be determined by the formula as follows:

$$I(t) = I_0 + A_1 \exp(-t/\tau_1) + A_2 \exp(-t/\tau_2) \quad (4)$$

$$\tau = \frac{A_1\tau_1^2 + A_2\tau_2^2}{A_1\tau_1 + A_2\tau_2} \quad (5)$$

where $I(t)$ and I_0 correspond to the emission intensity at time t and 0, respectively, A_J (J=1,2) is a constant, and τ_1 and τ_2 represent the decay times of the exponential components. The average decay lifetimes (τ) can be obtained by the eq. (5), the detailed results are listed in Table 2. The average decay lifetimes of $KNSNZ_x$ samples (x=0, 0.002, 0.005, 0.008, 0.010, 0.015) are 1.012 ms, 1.024 ms, 1.056 ms, 1.069 ms, 1.061 ms, and 1.046 ms, respectively. The chromaticity coordinates (CIE) and correlated color temperature (CCT) of samples with different Zr^{4+} content are calculated by a software (CIE1931xy.V.1.6.0.2) from the emission spectra, summarized in Table 2. The results show that the addition of Zr^{4+} ions almost has no effects on the chromaticity coordinates (x, y) and CCT, then does not change the emission color. In Table 2, the optimized composition with x=0.01 shows CIE chromaticity coordinates of (x = 0.5879, y = 0.4114) and a CCT of 1983 K, which is located in the orange region, closed to the edge of the CIE diagram, suggesting that the $KNSNZ_x$ materials have a high color purity.

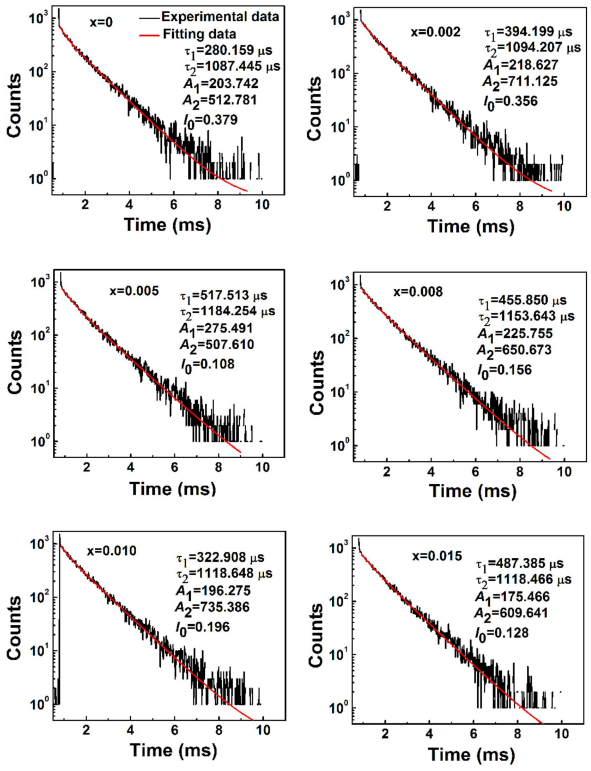

Fig. 9. The decay curves of the $KNSNZ_x$ ceramics at room temperature, the red curves are fitting results.

3.3. Thermal stability and water resistance behavior

Thermal quenching behavior of luminescent materials should be taken into accounts when materials are used in high-powered LEDs.[49] Thus, the temperature-dependent emission spectra of the $KNSNZ_x$ (x=0.01) sample excited by 407 nm are shown in Fig. 10. The temperature range is from 20 ºC to 260 ºC. The relative emission intensities normalized to the integral at 20 °C from the $^4G_{5/2} \rightarrow {}^6H_{7/2}$ transition as a function of temperature are given in the inset of Fig. 9. A slight increase of the emission intensity is observed with increasing temperature from 20 ºC to 60 ºC, owing to the effects of thermoluminescence.[50] Subsequently, the emission intensity gradually decreases with the temperature up to 260 ºC. However, the PL intensity still retains about 50% (at 140 ºC) of its initial intensity (at 20 ºC). Further increasing the measured temperature, the

phenomenon of thermal quenching appears. The luminescent center in the exited state can be activated by the temperature-dependence of the electron-phonon interaction. When the luminescent materials are subject to a high temperature, the $^4G_{5/2}$ state overcomes the energy barrier ΔE via the absorption of thermal activation energy, and releases nonradiatively to ground stated via a crossover between the $^6H_{5/2}$ ground state and $^4G_{5/2}$ excited states. At this time, the electron-phonon interaction plays a dominating role, then resulting in the decrease of emission intensity.[51] In order to clarify the thermal quenching behavior, the activation energy (E_a) can be determined by the Arrhenius equation:

$$I(T) = \frac{I_0}{1 + c\exp(-E_a / kT)} \quad (6)$$

where I_0 and $I(T)$ are the emission intensity at the initial temperature (20 °C) and the measured temperature T, c is a constant, E_a is the activation energy of thermal quenching, and k is the Boltzmann constant (8.629×10^{-5} eV/K).[52] According the Eq. (6), the E_a can be obtained from the slope of the fitting curves, i.e., $\ln[(I_0/I)-1]$ against $1/kT$, as indicated in Fig. 10(b). The thermal-quenching activation energy E_a was found to be approx. 0.706 eV.

In addition to thermal stability of luminescent materials, the water-resistant behavior must be considered as another important factor affecting the luminescent property of materials. Several results published in some literatures have confirmed that the luminescence intensity of some materials disappears rapidly after water treatment, due to hydrolysis, which severely limits some application of luminescence materials, especially in the biological field, for example, $Sr_{1-x}Al_2O_4:Eu_x$, $ZnS:Mn^{2+}$ luminescence materials.[53-55] Therefore, a material suitable for practical application not only possesses a high luminescence efficiency and thermal stability, but also a superior resistance to water. To verify the water resistance of the $KNSNZ_x$ system, the water

treatment experiments of the representative sample with x=0.01 mol were carried out at room temperature. The PL spectra of $KNSNZ_x$ (x=0.01) sample with various immersion times are shown in Fig. 11. The inset shows the dependence of the relative emission intensity ($^4G_{5/2}\rightarrow{}^6H_{7/2}$) on immersion time. After it is immersed in water, the sample with x=0.01 mol almost maintains the same PL intensity as before immersion. This independent behavior indicates that the crystalline structures of KNN-based ceramics is not destroyed after water treatment, which can be furher clarified by the XRD results (Fig. 2S). These results show that KNN-based luminescent materials co-doped with Sm^{3+} and Zr^{4+} are suitable for an application in an aqueous environment due to their superior water-resistant behavior.

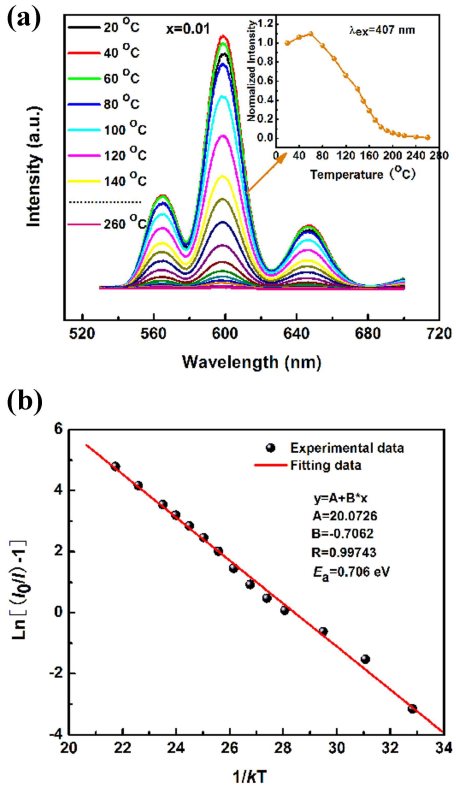

Fig. 10. (a) PL spectra (λ_{ex}=407 nm) of the $KNSNZ_x$ (x=0.01) ceramics at different temperatures in the range of 20 °C-260 °C, (b) the fitting curve of $Ln[(I_0/I_1)-1]$ vs. $1/T$.

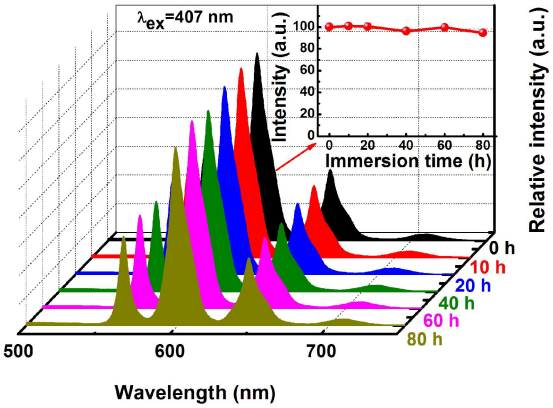

Fig. 11. PL spectra of $KNSNZ_x$ (x=0.01) sample with various immersion times. The inset shows the dependence of emission intensity ($^4G_{5/2}\rightarrow{}^6H_{7/2}$) on immersion time.

4. Conclusions

In this study, a series of orange light-emitting $KNSNZ_x$ (x=0, 0.002, 0.005, 0.008, 0.010, 0.015) samples were prepared by conventional solid state method. The phase structure, composition, photoluminescence property, thermal quenching and water resistance behavior were systematically investigated. The PL spectra showed that the KNN-based materials co-doped with Sm^{3+} and Zr^{4+} ions exhibited a strong orange emitting under the near-UV light excitation of 407 nm, which makes it compatible with all commercial n-UV LED chips (360-410 nm). The strongest emission peak was located at 597 nm, ascribed to the $^4G_{5/2}\rightarrow{}^6H_{7/2}$ transition. The introduction of Zr^{4+} ions significantly enhanced the emission intensity of Sm^{3+} ions due to the breaking of local crystal field symmetry and charge compensation. The emission intensity reached its maximum when Zr^{4+} doping content is about 0.01 mol. ions concentration. Meanwhile, the high QYs, good thermal ability and superior water resistance property make the $(K_{0.5}Na_{0.5})NbO_3:Sm^{3+}/Zr^{4+}$ materials a potential application in novel multifunctional devices, combined with its already admirable intrinsic piezoelectric properties.

Acknowledgments

This work was supported by the Natural Science Foundation of China (No. 51462028), the Natural Science Foundation of Inner Mongolia (No. 2014MS0522) and the Innovation Fund Project of Inner Mongolia University of Science and Technology (No. 2012NCL006 and 2012NCL002).

References

1 Y. Saito, H. Takao, T. Tani, T. Nonoyama, K. Takatori, T. Homma, T. Nagaya and M. Nakamura, Nature, 2004, 432, 84.

2 J. F. Li, K. Wang, F. Y. Zhu, L. Q. Cheng and F. Z. Yao, J. Am. Ceram. Soc., 2013, 96(12), 3677.

3 K. Wang and J. F. Li, Appl. Phys. Lett., 2007, 91, 262902.

4 F. Bortolani, A. D. Campo, J. F. Fernandez, F. Clemens and F. Rubio-Marcos, Chem. Mater., 2014, 26 (12), 3838.

5 F. Rubio-Marcos, A. D. Campo, R. López-Ju rez, J. J. Romero and J. F. Fernández, J. Mater. Chem., 2012, 22, 9714.

6. X. P. Wang, J. G. Wu, D. Q. Xiao, J. G. Zhu, X. J. Cheng, T. Zhang, B. Y. Zhang, X. J. Lou and X. J. Wang, J. Am. Chem. Soc., 2014, 136 (7), 2905.

7 Y. S. Sung, S. Baik, J. H. Lee, G. H. Ryu, D. Do, T. K. Song, M. H. Kim and W. J. Kim, Appl. Phys. Lett., 2012, 101, 012902.

8 S. Pin, F. Piccinelli, K. U. Kumar, S. Enzo, P. Ghigna, C. Cannas, A. Musinu, G. Mariotto, M. Bettinelli and A. Speghini, J. Solid. State Chem., 2012, 196, 1.

9 F. Z. Yao, E. A. Patterson, K. Wang, W. Jo, J. Rödel and J. F. Li, Appl. Phys. Lett., 2014, 104, 242912.

10 J, Fu, R. Z. Zuo, H. Qi, C. Zhang, J. F. Li and L. T. Li, Appl. Phys. Lett., 2014, 105, 242903.

11 L. Q. Cheng, K. Wang, J. F. Li, Y. M. Liu and J. Y. Li, J. Mater. Chem. C, 2014, 2, 9091.

12 K. Uchino, Piezoelectric Actuators and Ultrasonic Motors. Kluwer Academic Publishers, Boston, 1997.

13 W. Eerenstein, N. D. Mathur and J. F. Scott, Nature, 2006, 442, 759.

14 C. W. Nan, M. I. Bichurin, S. X. Dong, D. Viehland and G. Srinivasan, J. Appl. Phys., 2008, 103, 031101.

15. S. Ye, F. Xiao, Y. X. Pan, Y. Y. Ma and Q. Y. Zhang, Mater. Sci. Eng. R, 2010, 71, 1.

16 M. G. Wu, Y. Q. Lu and Y. X. Li, J. Am. Ceram. Soc., 2007, 90(11), 3642.

17 P. T. Diallo, P. Boutinaud, R. Mahiou, J. C. Cousseins and G. Srinivasan, Phys. Stat. Sol. (A), 1997, 160, 255.

18 X. S. Wang, C. N. Xu, H. Yamada, K. Nishikubo and X. G. Zheng, Adv. Mater., 2005, 17, 1254.

19 Y. Zhang and J. H. Hao, J. Mater. Chem. C, 2013, 1, 5607.

20 M.K. Tsang, G.X. Bai and J.H. Hao, Chem. Soc. Rev., 2015, 44, 1585.

21 R. López-Juárez, R. Castañeda-Guzmán, F. Rubio-Marcos, M. E. Villafuerte-Castrejón, E. Barrera-Calva, and F. González, Dalton Trans., 2013, 42, 6879.

22 H. Q. Sun, D. F. Peng, X. S. Wang, M. M. Tang, Q. W. Zhang and X. Yao, J. Appl. Phys., 110, 2011, 016102.

23 Y. B. Wei, Z. Wu, Y. M. Jia, J. Wu, Y. C. Shen and H. S. Luo, Appl. Phys. Lett., 2014, 105, 042902.

24 Q. L. Dai, H. W. Song, M. Y. Wang, X. Bai, B. Dong, R. F. Qin, X. S. Qu and H. Zhang, J. Phys. Chem. C, 2008, 112(49), 19399.

24 T. W. Kuo, W. R. Liu and T. M. Chen, 2010, 18(8), 8187.

26 N. Kimura, K. Sakuma, S. Hirafune, K. Asano, N. Hirosaki and R. J. Xie, Appl. Phys. Lett., 2007, 90, 051109.

27 J. H. Hao, Y. Zhang, and X. H. Wei, Angew. Chem., 2011, 123, 7008.

28 H. Zou, D. F. Peng, G. H. Wu, X. S. Wang, D. H. Bao, J. Li, Y. X. Li and X. Yao, J. Appl. Phys., 2013, 114, 073103.

29 S. K. Mahesh, P. P. Rao, M. Thomas, T. L. Francis and P. Koshy, Inorg. Chem., 2013, 52(23), 13304.

30 H. Q. Sun, D. F. Peng, X. S. Wang, M. M. Tang, Q. W. Zhang and X. Yao, J. Appl. Phys., 2012, 111, 046102.

31 Q. W. Zhang, H. Q. Sun, T. Kuang, R. G. Xing and X. H. Hao, RSC Adv., 2015, 5,4707.

32 G. X. Bai, Y. Zhang and J. H. Hao, J. Mater. Chem. C, 2014, 2, 4631.

33 D. M. Lin, K. W. Kwok and H. L. W. Chan, Appl. Phys. Lett., 2007, 90, 232903.

34 R. D. Shannon RD, Acta Crystallographica Section A: Crystal Physics, Diffraction Theoretical and General Crystallography, 1976, 32(5), 751.

35 E. Buixaderas, D. Nuzhnyy, I. Gregora, S. Kamba, M. Berta, B. Malič and M. Kosec, IEEE Transactions on Ultrasonics, Ferroelectrics, and Frequency Control, 2009, 56(9), 1843.

36 L. Q. Cheng, K. Wang, F. Z. Yao, F. Y. Zhu and J. F. Li, J. Am. Ceram. Soc., 2013, 96(9) 2693.

37 Z. G. Xia and D. M. Chen, J. Am. Ceram. Soc., 2010, 93(5), 1397.

38 P. L. Li, Z. J. Wang, Z. P. Yang, Q. L. Guo, and X. Li, Mater. Lett., 2009, 63 (9) 751.

39 W. T. Chen, H. S. Sheu, R. S. Liu and J. P. Attfield, J. Am. Chem. Soc. 2012, 134, 8022.

40 M. M. Jiao, Y. C. Jia, W. Lü, W. Z. Lv, Q. Zhao, B. Q. Shao and H. P. You, J. Mater. Chem. C , 2014, 2, 4304.

41 P. Ramasamy, P. Chandra, S. W. Rhee and J. Kim, 2013, 5, 8711.

42 B. Z. Malkin, A. A. Kaplyanskii and B. M. Macfarlane, Spectroscopy of Solids Containing

Rare earth Ions, North-Holland, Amsterdam, 1987, pp. 33–50.

43 J. G. Hao, W. F. Bai, B. Shen and J. W. Zhai, J. Alloys Compd., 2012, 534, 13.

44 S. Fujihara and K. Tokumo, Chem. Mater., 2005, 17(22), 5587.

45 W. N. Wang, W. Widiyastuti, T. Ogi, I. W. Lenggoro and K. Okuyama, Chem. Mater., 2007, 19, 1723.

46 Z. Y. Shen, Y. H. Zhen, K. Wang and J. F. Li, J. Am. Ceram. Soc., 2009, 92(8), 1748.

47 D. F. Peng, H. Q. Sun, X. S. Wang, J. C. Zhang, M. M. Tang and X. Yao, Mater. Sci. Eng. B, 2011, 176, 1513.

48 X. B. Qiao, Y. Cheng, L. Qin, C. X. Qin, P. Q. Cai, S. I. Kim and H. J. Seo, J. Alloys. Compd., 2014, 617, 946.

49 C. Feldman, T. Jüstel, C. R. Ronda and P. J. Schmidt, Adv. Funct. Mater., 2003, 13, 51.

50 J. C. Zhang, X. S. Wang and X. Yao, J. Alloys. Compd., 2010, 498, 152.

51 M. G. Brik, J. Phys. Chem. Solids, 2006, 67, 738.

52 S. Murakami, M. Herren, D. Rau and M. Morita, Inorg. Chim. Acta, 2000, 300-342, 1014.

53 Y. Imai, R. Momoda, Y. Adachi, K. Nishikubo, Y. Kaida, H. Yamada and C.N. Xu, J. Electrochem. Soc., 2007, 154, J77.

54 X. Lü, Mater. Chem. Phys., 2005, 93, 526.

55 L. Zhang, H. Yamada, Y. Imai and C. N. Xu, J. Electrochem. Soc., 2008, 155, J63.

Table 1. The photoluminescence properties and CIE chromaticity coordinates of KNN materials co-doped Sm^{3+} and Zr^{4+} ions

Samples	λ_{ex} (nm)	CIE		τ	CCT	QY
		x	y	ms	K	(η)
$(K_{0.5}Na_{0.5})_{0.99}Sm_{0.01}NbO_3$	407	0.5872	0.4121	1.012	1972	---
$(K_{0.5}Na_{0.5})_{0.99}Sm_{0.01}Nb_{0.998}Zr_{0.002}O_3$	407	0.5879	0.4114	1.024	1983	0.40
$(K_{0.5}Na_{0.5})_{0.99}Sm_{0.01}Nb_{0.995}Zr_{0.005}O_3$	407	0.5872	0.4121	1.056	1972	0.44
$(K_{0.5}Na_{0.5})_{0.99}Sm_{0.01}Nb_{0.992}Zr_{0.008}O_3$	407	0.5878	0.4115	1.069	1982	0.46
$(K_{0.5}Na_{0.5})_{0.99}Sm_{0.01}Nb_{0.990}Zr_{0.010}O_3$	407	0.5879	0.4114	1.061	1983	0.53
$(K_{0.5}Na_{0.5})_{0.99}Sm_{0.01}Nb_{0.985}Zr_{0.015}O_3$	407	0.5861	0.4132	1.046	1956	0.51
$Y_2O_3S:Eu^{3+}$ [Ref. 47]	394	***0.6220***	***0.3510***	--	--	0.35
$Y_2O_3:Eu^{3+}$ [Ref. 48]	465	***0.6550***	***0.3450***	--	--	<1%

Table 2. Chemical composition and K/Na mole ratio of the $KNSNZ_x$ (x=0.002, 0.010, 0.015) samples

Samples	Element (weight%)		Mole ratio
	K	Na	K/Na
$(K_{0.5}Na_{0.5})_{0.99}Sm_{0.01}Nb_{0.998}Zr_{0.002}O_3$	11.31	6.50	1.0230
$(K_{0.5}Na_{0.5})_{0.99}Sm_{0.01}Nb_{0.990}Zr_{0.010}O_3$	11.56	6.41	1.0604
$(K_{0.5}Na_{0.5})_{0.99}Sm_{0.01}Nb_{0.985}Zr_{0.015}O_3$	11.03	6.52	0.9947

Figures captions

Fig. 1. Schematic illustation of multiple functions of RE-doped ferro-/piezoelectrics.

Fig. 2 (a) The illustation of KNN with orthorhombic structure at room temperature [Ref. 3], (b) XRD patterns of $KNSNZ_x$ ceramics and (c) XRD patterns for the (200) and (020) peaks from 44° to 47.5°.

Fig. 3. IR spectra of the $KNSNZ_x$ (x=0, 0.002, 0.008, 0.015) at room temperature

Fig. 4. Weight percentage and K/Na mole ratio as a function of Zr^{4+} concentrations in $KNSNZ_x$ (x=0.002, 0.010, 0.015) ceramic samples.

Fig. 5. Room temperature PLE, PL and diffuse reflectance spectra of the $KNSNZ_x$ (x=0, 0.010) ceramics. The inset is the PL spectra of sample (x=0.10) excited by different wavelength.

Fig. 6. PL spectra of $KNSNZ_x$ ceramics excited by 407 nm at room temperature, the inset is the dependence of the emission intensity ($^4G_{5/2}\rightarrow{}^6H_{7/2}$) on Zr^{4+} concentrations.

Fig. 7. Variations of local crystal field and vacancy formation in KNN host co-doped with Sm^{3+} and Zr^{4+}, (a) x=0, (b) $x\leq 0.01$, (c) $x>0.10$

Fig. 8. PL spectra of the $KNSNZ_x$ (x=0.01) ceramics at different sintering temperature (a) and holding time (b) excited by 407 nm at room temperature, the insets show the dependence of emission intensity ($^4G_{5/2}\rightarrow{}^6H_{7/2}$) on sintering temperature and holding time.

Fig. 9. The decay curves of the $KNSNZ_x$ ceramics at room temperature, the red curves are fitting results.

Fig. 10. (a) PL spectra (λ_{ex}=407 nm) of the $KNSNZ_x$ (x=0.01) ceramics at different temperatures in the range of 20 °C-260 °C, (b) the fitting curve of $Ln[(I_0/I_1)-1]$ vs. $1/T$.

Fig. 11. PL spectra of $KNSNZ_x$ (x=0.01) sample with various immersion times. The inset shows the dependence of emission intensity ($^4G_{5/2} \rightarrow {}^6H_{7/2}$) on immersion time.